American Mineralogist, Volume 109, pages 1036–1044, 2024

Hydrogen incorporation mechanism in the lower-mantle bridgmanite

Narangoo Purevjav[1,2,†], Naotaka Tomioka[3], Shigeru Yamashita[1], Keiji Shinoda[4], Sachio Kobayashi[3], Kenji Shimizu[3], Motoo Ito[3], Suyu Fu[5], Jesse Gu[5,‡], Christina Hoffmann[6], Jung-Fu Lin[5], and Takuo Okuchi[1,7,*]

[1]Institute for Planetary Materials, Okayama University, Misasa 682-0193, Japan
[2]Bayerisches Geoinstitut, University of Bayreuth, 95440 Bayreuth, Germany
[3]Kochi Institute for Core Sample Research, X-star, Japan Agency for Marine-Earth Science and Technology (JAMSTEC), Nankoku, Kochi 783-8502, Japan
[4]Department of Geosciences, Graduate School of Science, Osaka Metropolitan University, Sugimoto 3-3-138, Sumiyoshi, Osaka 558-8585, Japan
[5]Department of Earth and Planetary Sciences, Jackson School of Geosciences, The University of Texas at Austin, Austin, Texas, U.S.A.
[6]Chemical and Engineering Materials Division, Neutron Sciences Directorate, Oak Ridge National Laboratory, Oak Ridge, Tennessee 37831, U.S.A.
[7]Institute for Integrated Radiation and Nuclear Science, Kyoto University, Kumatori, Osaka 590-0494, Japan

Abstract

Bridgmanite, the most abundant mineral in the lower mantle, can play an essential role in deep-Earth hydrogen storage and circulation processes. To better evaluate the hydrogen storage capacity and its substitution mechanism in bridgmanite occurring in nature, we have synthesized high-quality single-crystal bridgmanite with a composition of $(Mg_{0.88}Fe^{2+}_{0.05}Fe^{3+}_{0.05}Al_{0.03})(Si_{0.88}Al_{0.11}H_{0.01})O_3$ at nearly water-saturated environments relevant to topmost lower mantle pressure and temperature conditions. The crystallographic site position of hydrogen in the synthetic (Fe,Al)-bearing bridgmanite is evaluated by a time-of-flight single-crystal neutron diffraction scheme, together with supporting evidence from polarized infrared spectroscopy. Analysis of the results shows that the primary hydrogen site has an OH bond direction nearly parallel to the crystallographic *b* axis of the orthorhombic bridgmanite lattice, where hydrogen is located along the line between two oxygen anions to form a straight geometry of covalent and hydrogen bonds. Our modeled results show that hydrogen is incorporated into the crystal structure via coupled substitution of Al^{3+} and H^+ simultaneously exchanging for Si^{4+}, which does not require any cation vacancy. The concentration of hydrogen evaluated by secondary-ion mass spectrometry and neutron diffraction is ~0.1 wt% H_2O and consistent with each other, showing that neutron diffraction can be an alternative quantitative means for the characterization of trace amounts of hydrogen and its site occupancy in nominally anhydrous minerals.

Keywords: Bridgmanite, lower mantle, hydrogen substitution, neutron diffraction

Introduction

Chemically bonded hydrogen in rock-forming minerals of mafic oceanic lithospheres could survive subduction processes and be transported into the deep Earth via plate tectonic motions (Kawakatsu and Watada 2007; Ohtani et al. 2004; Thompson 1992). The total mass of such hydrogen cycle in the present Earth has been proposed to exceed the mass of surface ocean water (Karato et al. 2020). Crystal structures of hydrous and nominally anhydrous minerals in the deep Earth are possible candidates for transporting such hydrogen into the deep mantle. The hydrogen incorporation in these minerals can involve not only covalent hydroxyl (OH) bonds but also moderate to strong hydrogen bonds as determined primarily by neutron diffraction works (Purevjav et al. 2014, 2016, 2018, 2020; Sano-Furukawa et al. 2011, 2018; Tomioka et al. 2016; Trots et al. 2013; Suzuki et al. 2001). These hydrogen bonds in the host minerals allow hydrogen to stay in the host crystal structures even at relevant high-temperature conditions. Among such hydrogen-hosting minerals, wadsleyite and ringwoodite in the mantle transition zone from 410 to 660 km depth are among the most representative ones and relatively well documented; these minerals can have total water storage capacities as high as six ocean masses (Karato et al. 2020 and references therein). The actual existence of hydrogen in the transition zone had also been confirmed by the discovery of a natural hydrous ringwoodite crystal in a diamond inclusion (Pearson et al. 2014).

As for the fate of hydrogen beyond 660 km depth, it is essential to consider that some of the oceanic lithospheres can penetrate through the transition zone and carry some hydrogen into the lower mantle (Fukao et al. 2009; Fukao and Obayashi 2013; Portner et al. 2020). The lower mantle, the largest volume fraction of the layered Earth, consists of bridgmanite, ferropericlase, and other minor constituent phases. Bridgmanite likely represents ~80% of the lower-mantle volume (Hirose et al. 2017), such that hydrogen capacity and stability in this mineral phase is one of the primary factors in determining the distribution and

* Corresponding author E-mail: okuchi.takuo.2w@kyoto-u.ac.jp. Orcid 0000-0001-6907-0945
† Present address: School of Earth and Environmental Sciences, Seoul National University, Seoul 08826, Korea.
‡ Pressent address: Department of Earth and Planetary Sciences, Harvard University, Cambridge, Massachusetts 02138, U.S.A.

0003-004X/24/0006–1036$05.00/DOI: https://doi.org/10.2138/am-2022-8680

circulation of hydrogen within the multi-layered Earth. There have been extensive studies on hydrogen in bridgmanite in past decades, including analyses by Fourier transform infrared (FTIR) spectroscopy and secondary-ion mass spectrometry (SIMS) for synthetic crystals obtained at relevant high pressure and temperature conditions (Bolfan-Casanova et al. 2003; Litasov et al. 2003; Meade et al. 1994; Murakami et al. 2002; Liu et al. 2021; Panero et al. 2015). In addition to these studies, Fu et al. (2019) conducted a combined analysis of polarized FTIR and Nano-SIMS to characterize hydrogen in (Fe,Al)-bearing bridgmanite synthesized at nearly water-saturated, uppermost lower mantle conditions. They reported that the single-crystal bridgmanite, $Mg_{0.88}Fe^{3+}_{0.065}Fe^{2+}_{0.035}Al_{0.14}Si_{0.90}O_3$, contains ~1020(±70) ppm of H_2O and displays two pronounced OH^- stretching bands at ~3230 and ~3460 cm^{-1}. Following these works, here we have focused on the analysis of hydrogen's chemical bonding environments in the crystal structure of (Fe,Al)-bearing bridgmanite. For the first time, the high-quality bridgmanite crystals we synthesized here permit time-of-flight (TOF) Laue neutron diffraction analysis. These results allow us to refine the site of chemically bonded hydrogen and to model its cation exchange mechanism within the crystal structure. We have also conducted polarized FTIR analysis in all three principal crystal orientations. Together with SIMS analysis of the crystals, these results provide new insights in our understanding of the hydrogen substitution site and mechanism in the crystal structure of bridgmanite.

Crystal structure of bridgmanite and its hydrogen exchange mechanism

Here we briefly introduce the crystal structure of bridgmanite and its previously proposed hydrogen substitution mechanism as this information will be used to evaluate the actual experimental data for the hydrogen site occupancy in the present study. Figure 1 shows the crystal structure of (Fe, Al)-bearing bridgmanite (space group *Pbnm*), which is the same as that of $MgSiO_3$ bridgmanite (Horiuchi et al. 1987; Kudoh et al. 1990; Nakatsuka et al. 2021; Sugahara et al. 2006; Ross and Hazen 1989). The A cation site with 12 (or practically eight) oxygen anions (O^{2-}) is occupied by either magnesium (Mg^{2+}), iron ($Fe^{2+/3+}$), or aluminum (Al^{3+}). The B cation site with six O^{2-} anions is occupied by either silicon (Si^{4+}) or Al^{3+}. There are two O^{2-} sites (O1 and O2), which were proposed to include a minor fraction of vacant sites ($V_O^{\bullet\bullet}$) (Navrotsky 1999). Each O1 is shared by two BO_6 octahedra with the bonding direction along the *c*-axis, while each O2 is shared by two BO_6 octahedra with the bonding direction normal to the *c*-axis. Based on the aforementioned crystal structure, two types of hydrogen exchange mechanisms have been proposed for the Al-bearing bridgmanite system. These are: (1) Al^{3+} (or possibly Fe^{3+}) and H^+ simultaneously exchange for Si^{4+} at a B site (Muir and Brodholt 2018; Townsend et al. 2016), and (2) two Al^{3+} or Fe^{3+} and one $V_O^{\bullet\bullet}$ simultaneously exchange for two Si^{4+} at two B sites, and then some fraction of the generated $V_O^{\bullet\bullet}$ is coupled with another O^{2-} to simultaneously exchange for two OH^- (Litasov et al. 2003; Navrotsky 1999).

Experimental and analytical procedures

Synthesis

In the previous study, we synthesized high-quality, inclusion-free crystals of (Fe,Al)-bearing bridgmanite at a fixed pressure-temperature condition of 24 GPa and 1800 °C using a scaled-up Kawai-type cell (Fu et al. 2019; Okuchi et al. 2015). The current synthesis procedure was designed for growing larger crystals, several hundreds of micrometers in size, while maintaining the quality of the crystals. The starting material was made of a powder mixture of $MgSiO_3$, $Mg(OH)_2$, ^{57}FeO, and Al_2O_3, with 64.8, 20.2, 8.9, and 6.1 wt%, respectively. It contains 6 wt% of H_2O, simulating a water-saturated peridotite system. Approximately 15 mg of the mixture was packed into a Pt capsule with outer and inner diameters of 2.3 and 2.0 mm, respectively. The capsule was sealed by welding, inserted into a 14/6 Kawai-type cell assemblage, and then pressurized to 24 GPa by applying a 19 MN load at the Institute for Planetary Materials (IPM), Okayama University. At the targeted pressure, the capsule was heated to 1820 °C and kept for 10 min to melt the mixture. Then, the temperature was slowly reduced to 1690 °C with a cooling rate of 0.5 °C/min for 4 h, and even more slowly decreased to 1590 °C with a rate of 0.1 °C/min for 12 h. Finally, the temperature was kept constant for another 4 h. After this series of temperature control procedures, the sample was quenched by cutting off the power source under high pressure. The assemblage was then decompressed to ambient pressure.

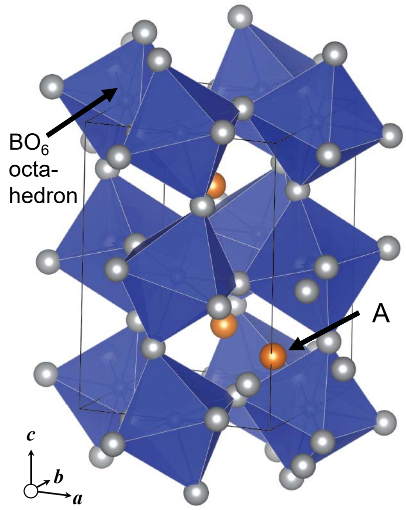

Figure 1. The crystal structure of (Fe,Al)-bearing bridgmanite with an orthorhombic symmetry (space group *Pbnm*). The bridgmanite structure consists of A-site cations, B-site cations, and oxygen anions with an ABO_3 perovskite-type framework. In the illustration, the A sites are visible as brown spheres while the B sites are hidden inside blue-colored BO_6 octahedra. The illustration was produced using VESTA3 (Momma and Izumi 2011). (Color online.)

Phase identification and major element analysis

After decompression and recovery of the product crystals from the capsule, several crystals were selected and analyzed using micro-focused XRD (Rigaku's RINT RAPID II-CMF) at IPM. The largest dark brownish bridgmanite crystals were ~500 μm in size (Fig. 2a). A small fraction of transparent majorite crystals of ~200 μm sizes were also found to coexist with the bridgmanite. Fine-powdered and light-greenish quenched aggregates were also occasionally found, which were identified by XRD analysis as a mixture of dense hydrous magnesium silicate (DHMS) phase D and brucite. This indicates that the bridgmanite crystals were grown in a nearly water-saturated magmatic environment (Fig. 2b).

Major-element compositions of the bridgmanite crystals were determined using a JEOL JXA-8800 electron-probe microanalyzer (EPMA), with operating conditions of 15 kV accelerating voltage, 12.1 nA probe current, and 5 μm probe diameter. Two crystals with polished surfaces were measured by taking four data points from each crystal (Table 1). In addition to these point analyses, macroscopic chemical homogeneity of Mg, Si, Fe, Al, and O within these crystals was confirmed by map analysis. An additional double-side polished crystal 190 × 170 $μm^2$ in size and ~200 μm in thickness was prepared for Mössbauer spectroscopy of ^{57}Fe analysis at Advanced Photon Source at the Argonne National Laboratory (Fig. 2c). Ferric iron fraction of the bridgmanite crystal was determined to be $Fe^{3+}/\Sigma Fe$ = ~52% (Fig. 2d). Based on these results, the major-element chemical formula of

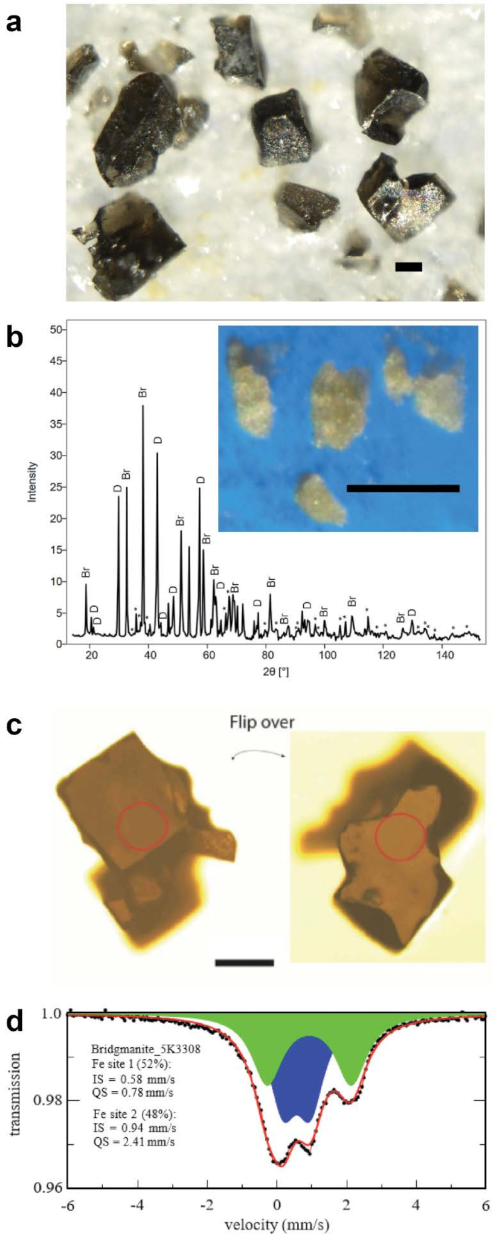

Figure 2. Synthesis and characterization of the (Fe,Al)-bearing bridgmanite crystals. All scale bars shown with black color are 100 μm in length. (**a**) A stereo microscope image of the recovered bridgmanite crystals with dark-brownish color and subhedral to euhedral forms. (**b**) A micro-focused X-ray diffraction pattern of the recovered aggregates with a mixture of the bridgmanite (asterisks), brucite (Br), and DHMS phase D (D), indicating that the bridgmanite crystals were grown under nearly water-saturated condition. The inset shows the appearance of the aggregates. (**c**) Double-side polished crystal of the (Fe,Al)-bearing bridgmanite with a thickness of ~200 μm. The red circles indicate the areas for Mössbauer measurements. (**d**) Mössbauer spectrum of the bridgmanite crystal. The spectrum was collected using a ^{57}Co point source with a beam size of 300 μm and a collection time of ~40 h. The spectrum was fit with two doublets, corresponding to Fe^{2+} (green) and Fe^{3+} (blue) using the MossA program (Prescher et al. 2012). Analysis of the spectrum shows ~52% $Fe^{3+}/\Sigma Fe$ and ~48% $Fe^{2+}/\Sigma Fe$. (Color online.)

bridgmanite was defined as $Mg_{0.88}Fe^{2+}_{0.05}Fe^{3+}_{0.05}Al_{0.11}Si_{0.88}O_3$ including all the cation species except hydrogen.

Transmission electron microscopy

Four bridgmanite crystals of 200–400 μm size were prepared for transmission electron microscopy (TEM) analysis. They were cross-sectioned and polished to prepare for five independent foils of 100 to 150 nm in thicknesses and lateral sizes of ~12 × ~8 μm^2, using a Hitachi SMI-4050 focused ion beam apparatus. Figure 3 shows representative TEM images of one of the foils using JEOL JEM-ARM200F at the Japan Agency for Marine-Earth Science and Technology (JAMSTEC), which was operated at low magnification TEM mode (Fig. 3a) and high-resolution scanning TEM (HR-STEM) mode (Figs. 3b and 3c) at 200 kV accelerating voltage. Nanoscale analysis of the samples shows that they are homogeneous and free of inclusions and defects, indicating that hydrogen must be incorporated in the lattice instead of forming precipitates or inclusions within the crystal. The selected-area electron diffraction patterns also feature sharp spots consistent with a long-range ordered high-quality crystal structure (Fig. 3d).

Polarized Infrared and SIMS analysis

Using polarized FTIR spectroscopy, we determined the bonding direction and strength of structural hydroxyls (OH^-) within the three-dimensional lattice of the (Fe,Al)-bearing bridgmanite (Fig. 4). Three crystals of ~400 μm sizes were selected for determination of their crystallographic orientations using X-ray precession photography at Osaka Metropolitan University (Figs. 4e and 4f). Double-side polished thin sections of thicknesses from 100 to 350 μm were prepared to have orientations normal to the three crystallographic axes of bridgmanite. FTIR spectra of the three sections were taken at IPM using a JASCO FTIR-6200 spectrometer coupled to an IRT-7000 microscope with 10× objective/condenser, a KBr/Ge beamsplitter, an MCT detector, a ceramic infrared light source, and a KRS-5/Al wire-grid polarizer. A series of polarized spectra were collected within each section, where 1024 scans were accumulated in each spectrum with an aperture size of 50 × 50 μm and a wavenumber resolution of 4 cm^{-1}. Considering the limit of page space, two spectra series from sections normal to *a* and *c* axes are shown in detail, which are essential to determine the orientation of the O-H dipoles (Figs. 4a and 4b). Nonlinear peak fitting analysis was conducted for these series to model each band. Pole figures were prepared to show the two most important bands within the two spectra series (Figs. 4c and 4d). These spectra within each crystal were highly reproducible at several different aperture positions, indicating the homogeneous distribution of hydrogen within the crystal.

The hydrogen concentration was quantitatively analyzed by SIMS (CAMECA IMS-6F) at JAMSTEC. The other three crystals of ~250 μm sizes were embedded in an indium pellet together with standard materials. Sample mounts were ultrasonically washed using acetone and pure water and then dried in a vacuum oven overnight before coating. The mount was then coated with gold of 30 nm thickness and kept in a SIMS sample chamber in a vacuum for more than a day before the analysis. This procedure worked effectively to reduce the background of absorbed water on the sample surface. In the SIMS measurements, a primary $^{133}Cs^+$ beam operated at 1 nA and 14.5 keV was focused to a 15 μm spot on the sample surface. Normal incident electron shower was used for electrostatic charge neutralization of the sputtering area. A field aperture was used to permit transmission of ions from the central area of 10 μm in diameter of the sputtered region to minimize the hydrogen signals from remaining absorbed water on the sample surface. The secondary ions of ^1H, ^{12}C, and ^{30}Si were collected from the sputtered area sequentially by an electron multiplier with 1 s × 20 cycles. Total duration of each analysis was ~5 min, including 120 s of pre-sputtering. For hydrogen standard materials, we used: (1) natural amphibole from the Ichinomegata volcano (Miyagi and Yurimoto 1995) and (2) aphyric glass of a mid-oceanic ridge basalt EPR-G3 from the East Pacific Rise (Shimizu et al. 2017), which were reported to contain 1.66 and 0.22 wt% of H_2O, respectively (Fig. 5). As for the dry silicate standard for background analyses of hydrogen and carbon, San Carlos olivine was used. While we measured ^{12}C for monitoring contaminations from invisible scratches or cracks on the minerals, we did not observe any irregularly higher $^{12}C/^{30}Si$ ratios than the carbon background. To determine the hydrogen concentration in sample crystals, five to seven data points were collected from different portions of each crystal, where we once again confirmed that hydrogen was homogeneously distributed within these crystals, as in the case of FTIR results. Figure 5 shows our procedure to determine the hydrogen concentration as H_2O in the samples, assuming a linear relationship between their concentrations and the $^1H/^{30}Si$ ratio. We did not conduct background correction of H_2O because the observed $^1H/^{30}Si$ ratio of San Carlos olivine was negligibly small compared

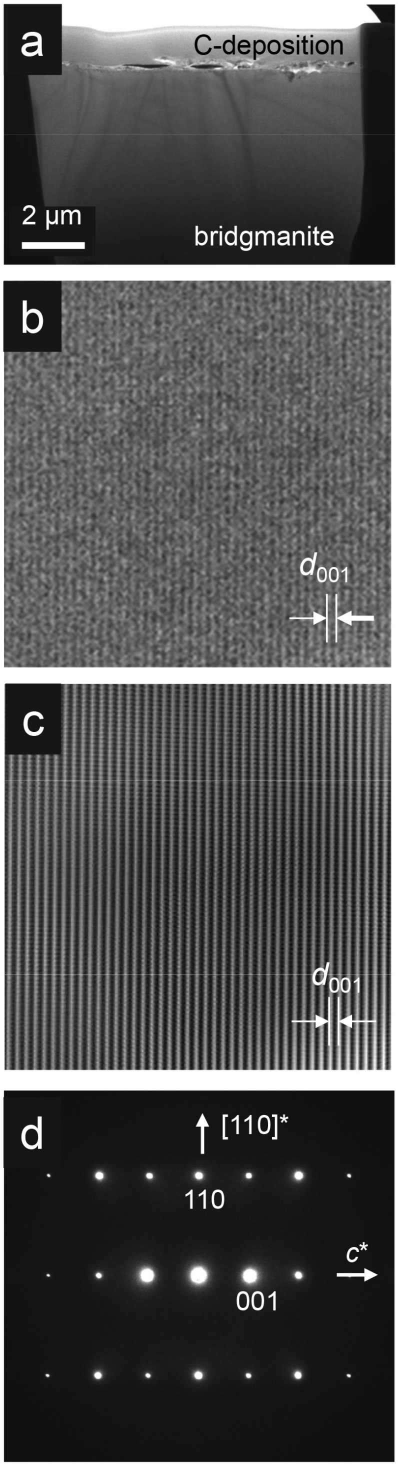

FIGURE 3. TEM/STEM micrographs of the (Fe,Al)-bearing bridgmanite crystal. (**a**) A bright-field TEM image of a representative thin foil, which shows homogeneous crystal without visible inclusions or defects. (**b**) A bright-field STEM image showing the lattice fringes of (001). (**c**) A Fourier-noise-filtered image of **b**, which confirmed high-quality lattice spaces without disturbances. (**d**) A selected-area electron diffraction (SAED) pattern along the [$1\bar{1}0$] zone axis of the crystal. The SAED pattern shows sharp reflection spots of the bridgmanite structure.

with the sample crystals. The H_2O concentration in the bridgmanite was either 630(40) or 810(50) ppm: the former was obtained using the natural amphibole standard, and the latter was obtained using the EPR-G3 glass. These results are compared with the neutron diffraction results that are described later in this paper.

Neutron diffraction and major element distribution

As collaboratively demonstrated by the data sets of EPMA, HR-(S)TEM, FTIR, and SIMS analyses, the synthesized (Fe,Al)-bearing bridgmanite crystals were chemically homogeneous in their major cations and hydrogen distributions (Okuchi et al. 2015). In the present study, we aim to refine the site position of hydrogen in the bridgmanite crystal structure, where neutron diffraction plays the most essential role. To achieve the task, it is essential to find site distributions and occupancies of all major cations and anions in addition to hydrogen, because hydrogen can only become visible after removing all scattering densities of these stronger neutron scatters from the bridgmanite lattice space. One of the largest crystals was selected for neutron diffraction, which was $0.4 \times 0.5 \times 0.15$ mm^3. The crystal was exposed to the neutron beam for ~2.5 days in total at a TOF Laue diffractometer TOPAZ installed at the Spallation Neutron Source (SNS), Oak Ridge National Laboratory, which was operated at 1.4 MW proton beam power (Schultz et al. 2014). The crystal was cooled down to 100 K by cold nitrogen gas, where the signal-to-noise ratio of higher-order reflections was enhanced (Purevjav et al. 2016, 2018, 2020). For covering the full reciprocal space, we sequentially reoriented the crystal to have 25 different orientations with the help of the CrystalPlan software (Zikovsky et al. 2011). The obtained *hkl*-intensity data set was refined using the General Structure Analysis Software (Larson and Von Dreele 2004). The optimized structure parameters are summarized in Table 2. The refined space group of the bridgmanite crystal is *Pbnm*, consistent with the previous studies. The lattice constants determined at 100 K are $a = 4.8071(2)$ Å, $b = 4.9473(1)$ Å, and $c = 6.9141(2)$ Å. The CIF[1] is available.

Based on the EPMA analysis, we have obtained the total occupancies of A and B sites for Mg, Fe, Al, and Si cations. Upon defining their relative distributions between A and B sites (Fig. 1), we considered their preferences reported in the previous crystal-chemical studies of aluminous and/or ferrous bridgmanite: (1) Mg and Fe strongly prefer the A site; (2) Si strongly prefers the B site; and (3) Al moderately prefers the B site, which is all due to the relations between the relevant site volumes and ionic radii (Lin et al. 2016; Nakatsuka et al. 2021; Nishio-Hamane et al. 2005). In addition, Al can be distributed into the A site when the capacity of the B site is exceeded, as confirmed by the stability of the bridgmanite structure along the solid solution of $MgSiO_3$ and $Mg_3Al_2Si_3O_{12}$ (Hirose et al. 2001; Kubo and Akaogi 2000). Therefore, in our structural refinements, Mg and Fe were all fixed in the A site, and Si was fixed in the B site, whereas Al occupancies were refined between the A and B sites while constraining their total to be equal with the bulk analytical result from EPMA. As shown in Table 2, this constrained refinement procedure for cation occupancies provided a very reasonable solution: the neutron coherent scattering length of ^{57}Fe (= 2.3), Al (= 3.45), Si (= 4.15), and Mg (= 5.38) are all substantially different from each other, guaranteeing that their site distribution was solidly constrained as long as the scattering intensity dataset had enough quality. We found that the total occupancy of the A site was 1.01 as the sum of Mg, Fe, and Al nuclear site occupancies, whereas its total cation charge was 2.11 as the sum of Mg^{2+}, Fe^{2+}, Fe^{2+}, and Al^{3+} valences. We also found that the total occupancy of the B site was 0.99 as the sum of Al and Si nuclear site occupancies, where its total cation charge was 3.84 as the sum of Al^{3+} and Si^{4+} valences. The total cation valence charge at the A and B sites was $2.11 + 3.84 = 5.95$, which was smaller than the total anion charge of 6.00, as necessarily expected when hydrogen cations were additionally involved within the crystal structure. From these results on the nuclear site occupancies, we concluded that Fe^{2+} or Fe^{3+} did not substantially exist in the B site, which was in contrast to some previous reports (Frost and Langenhorst 2002; Hummer and Fei 2012; Litasov et al. 2003). We note that the results were obtained along with the refined scale factor that assured full occupancies of the two oxygen sites (Table 2). Unreasonable cation site deficiencies in both the A and B sites would be necessary if we instead assumed nontrivial oxygen site vacancies, as previously proposed (Navrotsky 1999).

Neutron diffraction and hydrogen site analysis

Normal hydrogen (^{1}H) generates negative scattering length density distribution of neutrons, whereas all other atoms generate positive densities. Therefore, even if the concentration of hydrogen is much smaller than the other atoms, its position can still be detectable as a unique negative anomaly in the three-dimensional scattering density map (Fourier map). To find such an anomaly in our data, we obtained a difference-Fourier map similar to the case of our previous

TABLE 1. Major-element composition of two representative bridgmanite crystals analyzed by EPMA

Crystal	1					2					1 and 2
Point	1	2	3	4	average	1	2	3	4	average	average[a]
SiO_2	51.6	51.5	52.0	51.9	51.8(2)	49.4	51.2	51.3	50.9	50.7(9)	51.2(8)
Al_2O_3	7.1	7.5	7.1	6.9	7.1(3)	6.8	7.5	7.6	7.5	7.4(4)	7.2(3)
MgO	34.7	34.5	34.6	34.7	34.6(1)	33.6	34.6	34.4	34.3	34.2(5)	34.4(4)
FeO*	6.6	6.8	6.5	6.5	6.6(1)	8.9	7.1	7.2	7.1	7.6(9)	7.1(8)
Total	100.0	100.3	100.2	99.9	100.1(2)	98.6	100.5	100.5	99.7	99.8(9)	100.0(6)

Notes: The weight percent of each oxide component is listed, where FeO* is determined assuming all Fe is Fe^{2+}. [a] Total average values of the two crystals were used for the neutron structure refinement.

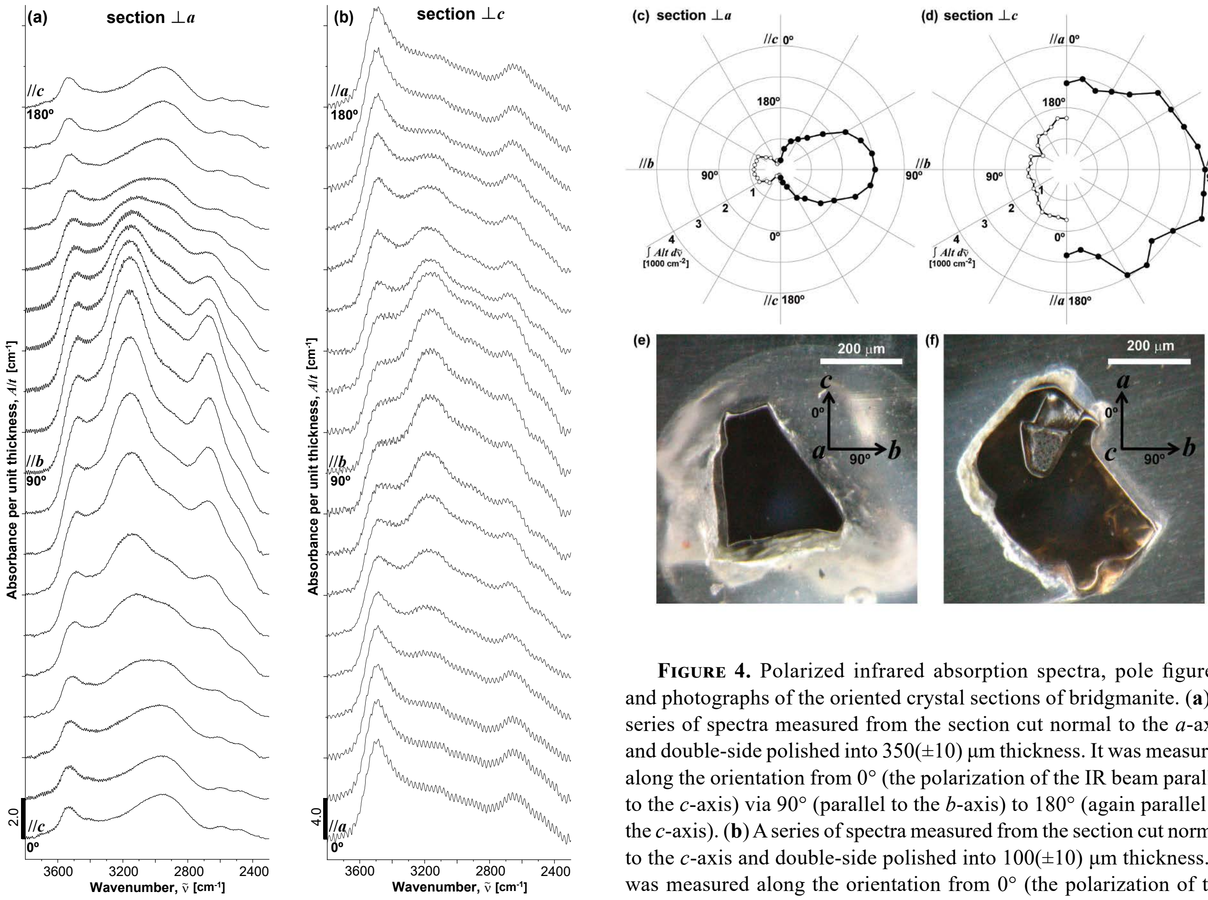

FIGURE 4. Polarized infrared absorption spectra, pole figures, and photographs of the oriented crystal sections of bridgmanite. (**a**) A series of spectra measured from the section cut normal to the *a*-axis and double-side polished into 350(±10) μm thickness. It was measured along the orientation from 0° (the polarization of the IR beam parallel to the *c*-axis) via 90° (parallel to the *b*-axis) to 180° (again parallel to the *c*-axis). (**b**) A series of spectra measured from the section cut normal to the *c*-axis and double-side polished into 100(±10) μm thickness. It was measured along the orientation from 0° (the polarization of the IR beam parallel to the *a*-axis) via 90° (parallel to the *b*-axis) to 180° (again parallel to the *a*-axis). (**c** and **d**) The couple of pole figures corresponding to the series of spectra **a** and **b**. These show intensity trend of integrated absorbances of 3480 cm^{-1} (open circle) and 3160 cm^{-1} (filled circle) bands, respectively. (**e** and **f**) The measured crystal sections cut normal to the *a* and *c* axes, respectively. For each spectrum shown in **a** and **b**, a baseline for the window of O-H stretching region (2300 to 3800 cm^{-1}) was defined as a spline function covering the original spectrum from 1500 to 4000 cm^{-1}, and was subtracted from the original. This baseline was close to linear in the window of the O-H stretching region. For defining each point shown in **c** and **d**, a nonlinear peak-fitting analysis was conducted to resolve overlapped Gaussian peaks within the series of spectra **a** and **b**. (Color online.)

work (Purevjav et al. 2018). We calculated this map using the difference between all major cation and anion densities and the observed neutron scattering densities. To discriminate the hydrogen site, we refined the coordinates, the occupancy, and the Debye-Waller factors of each candidate position step-by-step, as suggested from each apparently negative anomaly in the difference map. These procedures in finding the candidate site were made for 63 candidate positions located at distances of 0.7 to 1.3 Å measured from the nearest oxygen site. As explained later in the discussion, only one of them, shown in Figure 6, was fully consistent with the other analytical results, such that we defined it as the primary hydrogen site shown in Table 2.

Neutron diffraction and hydrogen concentration

After finding the primary site, we try to evaluate its occupancy, which is equivalent to the hydrogen concentration in the crystal structure. This is a much more challenging task than finding the site because of its small occupancy, low site symmetry, and very large Debye-Waller factors, which all consistently make the quantitative evaluation of scattering density of hydrogen difficult. We previously reported that the accuracy of refined hydrogen occupancy is secured by its stability as a function of resolution in space, where the resolution increases with increasing number of reflections at smaller *d*-spacings (Purevjav et al. 2016, 2018). Following this methodology, we evaluated the hydrogen occupancy in bridgmanite (Fig. 7).

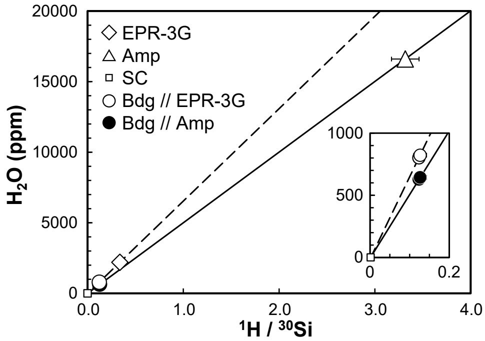

Figure 5. Results of hydrogen concentration analysis for the bridgmanite (Bdg) crystals by SIMS. The solid and broken lines show correlations between $^1H/^{30}Si$ count ratios and water concentrations using natural amphibole (Amp) and basaltic glass (EPR-3G) as the standards, respectively. San Carlos olivine (SC) was used as the dry reference standard. Two independent H_2O concentrations from the two crystals (an enlarged region is shown in the inset) were obtained using the averages of all data points from each crystal.

It was proved to be stable throughout the whole resolution range to provide best-effort site occupancy of 0.010 ± 0.003 (Table 2).

Results and discussion

Primary site position deduced from infrared and neutron results

Using the polarized FTIR results, here we discuss the most-plausible hydroxyl bonding strength and direction in the bridgmanite. It was suggested that multiple bonding geometries coexisted within the crystal structure because of such broad and orientation-dependent infrared absorption profiles, which ranged from 2300 to 3800 cm^{-1} (Fig. 4). The bonding geometries must also be highly anisotropic within the bridgmanite structure. By carefully evaluating the orientational dependence of the profiles, we assigned four coexisting vibration bands, which have peak wavenumbers at 3480(±40), 3160(±20), 2880(±20), and 2680(±50) cm^{-1}, respectively. The integrated area intensity of the 3160 cm^{-1} band was much more significant than the 3480 cm^{-1} band (Figs. 4c and 4d) and also than the other two. Therefore, even considering the negative correlation between the molar absorption coefficient and the OH stretching wavenumber (Libowitzky and Rossman 1997), the most intense 3160 cm^{-1} band still showed the property of the most important hydrogen site. The next strongest 3480 cm^{-1} band showed the property of the second site. When the section normal to the *a* axis was analyzed (Fig. 4c), these two bands had common strong pleochroism with the largest absorbances along the *b* axis and very small absorbances along the *c* axis. Therefore, both of these OH dipoles were oriented normal to the *c*-axis. When the section normal to the *c* axis was analyzed (Fig. 4d), the two bands showed reversing moderate pleochroism. While the 3160 cm^{-1} band showed the largest absorbance around the *b* axis, the 3480 cm^{-1} band showed the largest absorbance around the *a* axis. Their wavenumbers were reported to quantitatively reflect hydrogen bonding strength; it is reasonable to assume that the 3160 cm^{-1} band was from hydroxyls with a moderately strong hydrogen bond, while the 3480 cm^{-1} band was from that with a very weak hydrogen bond (Libowitzky 1999). While the crystal orientation information was less clarified than in the current case, the coexistences of these two bands and their coherent behavior against crystal orientation were already observed by infrared analysis of (Fe,Al)-bearing bridgmanite (Fu et al. 2019; Litasov et al. 2003). Considering the features of the two strong bands, we conclude that the most important hydrogen site formed hydroxyls approximately aligned along the *b*-axis with moderately strong hydrogen bonding, whereas the second site approximately aligned along the *a*-axis with very weak hydrogen bonding.

With the new insights from these infrared results, it follows that the primary hydrogen site is located between two O1 oxygen anions, which is the most consistent solution among the possible candidates suggested from the neutron diffraction results. These two O1 O atoms form an edge of the A site dodecahedron, where the hydrogen is installed with a hydrogen bonding angle of 179(6)° (Fig. 6), forming a straight bonding geometry along the edge. The covalent hydroxyl bond has a distance of 1.03(7) Å, and the counterpart hydrogen bond has a distance of 1.81(7) Å. The hydrogen sites related to the other three bands at 3480, 2880, and at 2680 cm^{-1} are not yet clearly resolved by neutron diffraction. Nonetheless, they show substantial pleochroism as a function of orientation, making them definable as independent bands. We currently do not have any conclusive solution on their crystallographic geometry. A suggestion may come from previous infrared evidence for another nominally anhydrous mineral having an octahedrally coordinated Si cation site. For example, a remarkably similar infrared band of very weak absorption at 2659–2667 cm^{-1} was reported for both Al-free and Al-bearing stishovite, where either reaction of $Si^{4+} \leftrightarrow Al^{3+} + H^+$ or $Si^{4+} \leftrightarrow 4H^+$ was proposed to generate its wide variety of hydroxyl absorption bands (Litasov et al. 2007). In addition, a combination of two

Table 2. Refined structure parameters of the (Fe, Al)-bearing bridgmanite

Wyckoff positions	Atoms	Coordinates			Occupancies	Debye-Waller factors (×10²), Å²						
		x	*y*	*z*		U_{11}	U_{22}	U_{33}	U_{12}	U_{13}	U_{23}	U_{iso}
4*b* (A-site)	Mg Fe Al	0.51446(7)	0.55654(5)	0.25	0.877 0.101 0.034(1)		0.370(10)	0.352(7)	0.601(8)	0.080(7)	0	0
4*b* (B-site)	Si Al	0.5	0	0	0.875 0.113(1)	0.150(10)	0.143(8)	0.174(8)	0	0	0.013(6)	
4*c*	O1	0.10543(5)	0.46321(4)	0.25	0.998(1)	0.346(8)	0.356(6)	0.320(6)	0	0	0	
8*d*	O2	0.19497(4)	0.20015(3)	0.55449(2)	1.000(1)	0.365(6)	0.372(4)	0.419(5)	0.070(4)	0.069(4)	0.084(4)	
4*c*	H	0.288(14)	0.143(13)	0.25	0.010(3)							3(1)

Notes: Initial atomic coordinates in the refinements were taken from Horiuchi et al. (1987). See the text for the refinement procedure in detail.

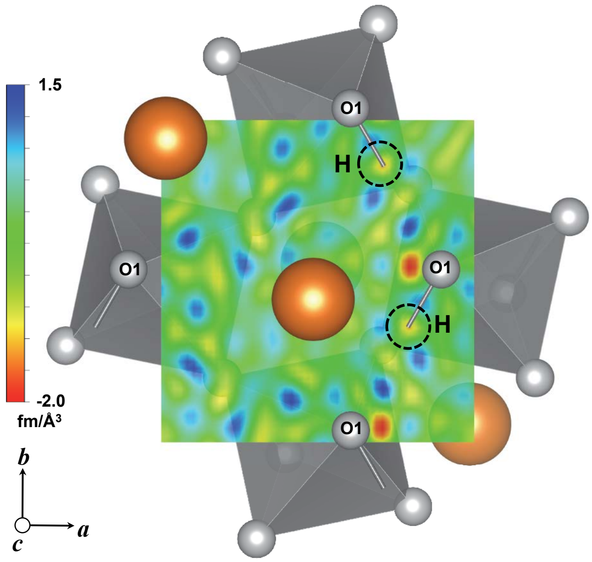

Figure 6. A difference-Fourier map sectioned normal to the *c*-axis of the bridgmanite. The map shows residual nuclear density distribution after removing scattering contributions from all major cations and anions other than hydrogen. The A sites (shown in brown color) are occupied by Mg, Fe, and Al cations, whereas the B sites (shown in gray color) are occupied by Al and Si cations. This map simultaneously shows positive (blue color) and negative (yellow and red colors) residuals of the scattering density. We evaluated each of the apparent negative residual in the three-dimensional map volume, including those not shown in this section, for finding the possible hydrogen site position (see the text for details). After the evaluation, a negative residual of –1.16 fm/Å^3, as highlighted by the black-dashed circle, was determined as the primary hydrogen site position. The hydrogen is located between two O1 oxygen anions, with OH covalent bonding direction close to the *b* axis. (Color online.)

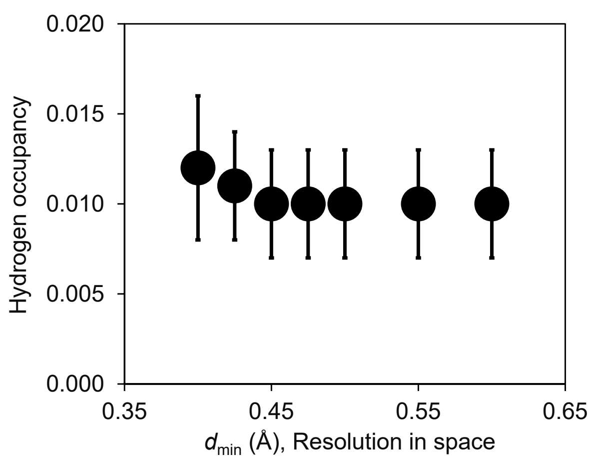

Figure 7. The refined hydrogen site occupancies as a function of the resolution in space. The hydrogen site was refined as (x, y, z = 0.288, 0.143, 0.25) (see Table 2). These occupancies were determined one by one for a series of reflection intensity data sets with different minimum *d*-spacings from 0.40 to 0.60 Å.

broad but distinct bands at around 2900 and 2650 cm^{-1} were reported to exist in Al-free stishovite experiencing $Si^{4+} \leftrightarrow 4H^+$ hydration reaction (Spektor et al. 2016). Thus, the bands at the lower wavenumbers observed in bridgmanite could come from clustered hydrogen around the vacant B site, although further studies are necessary to clarify the nature of such hydrogen clusters in the crystal structure of bridgmanite.

Hydrogen substitution mechanism

In previous works using neutron diffraction, we successfully determined the full structure parameters of several dense hydrogen-bearing minerals occurring in the mantle transition zone, including both nominally hydrous and anhydrous types (Purevjav et al. 2014, 2016, 2018, 2020). It has been demonstrated that octahedrally coordinated Mg^{2+} or Fe^{2+}, as well as tetrahedrally coordinated Si^{4+}, were removed to exchange for hydrogen. That is, hydrogen clusters are generated around the sites originally filled by Mg^{2+}, Fe^{2+}, and Si^{4+} cations. On the other hand, in the bridgmanite structure in the lower mantle, these major cations remain even after the hydration reaction. In other words, it is preferred to avoid creating any cation vacancy as well as hydrogen clusters. By simply referring to the total cation occupancy of 1.01 and its valence charge of 2.06 in the A site, it is clear that hydrogen clustering around such a fully filled site with such an excess charge is energetically unfavorable. We thus conclude that one hydrogen around one filled cation is the unique solution most consistent with the neutron diffraction result (Fig. 6; Table 2). On the other hand, the total cation charge of 3.94 in the B site must be compensated by such an addition of hydrogen around oxygen anions surrounding the site. Since Al^{3+} causes the smaller charge in the B site, the major hydrogen exchange reaction in (Fe,Al)-bearing bridgmanite must be (1) Al^{3+} and H^+ simultaneously exchanging for Si^{4+} in the B site (Muir and Brodholt 2018; Townsend et al. 2016). We note that the addition of hydrogen only increases the total cation charge to 5.96, which is still smaller than the total anion charge of 6.00. The origin of the remaining difference (0.04 per formulation) is still not clear; it is not reasonable to assume a far larger concentration of hydrogen in this site, as explained later. While we may ascribe some fraction of this difference by possible uncertainty of EPMA analysis and Mössbauer results, further research is necessary to solve this issue of the missing cation valence charge.

Hydrogen concentration

To provide a reliable hydrogen concentration in aluminous bridgmanite, which has been greatly debated so far (Fu et al. 2019; Litasov et al. 2003; Liu et al. 2021; Murakami et al. 2002), and also to evaluate the technical limit of single-crystal neutron diffraction for a trace amount of hydrogen, we finally compare and discuss the concentration values obtained by neutron diffraction and SIMS schemes to each other. Our SIMS results show that the H_2O concentration is between 630(±40) and 810(±50) ppm (Fig. 5). On the other hand, our neutron diffraction results show that the hydrogen site occupancy is 0.010(±0.003), which corresponds to its bulk concentration of 870(±260) ppm (Fig. 7). These results are rather consistent with each other, suggesting that single-crystal neutron diffraction can be an alternative means for a quantitative evaluation of hydrogen concentration as low as 900 ppm = 0.09 wt% of H_2O. We also note that our infrared results suggest the existence of minor hydrogen site(s), which were not revealed in the analysis of neutron diffraction data, but could still be detected in the SIMS analysis results. Further neutron diffraction research using even larger crystals with significantly larger volumes could be useful to address other remaining questions in hydrated bridgmanite.

Implications and conclusions

In this study, we have determined the full crystallographic parameters of hydrous (Fe,Al)-bearing bridgmanite, including its hydrogen site position and occupancy, using the TOF Laue neutron diffraction scheme. The diffraction experiments proved successful due to the use of large and high-quality bridgmanite crystal synthetically grown in a nearly water-saturated environment. Together with the complementary dataset of polarized infrared spectroscopy, our results show that both the hydroxyl covalent bond and the hydrogen bond are directed nearly parallel to the crystallographic *b*-axis. The water concentration in bridgmanite has been quantitatively evaluated by SIMS analysis, in addition to the neutron diffraction scheme. These results for water concentration are self-consistent and complementary to each other, showing that neutron diffraction can be used to detect its trace amount as low as ~0.1 wt% H_2O.

It was demonstrated that hydrogen is incorporated into the bridgmanite structure via the coupled exchange reaction of H^+ and Al^{3+} for Si^{4+} ($H^+ + Al^{3+} \leftrightarrow Si^{4+}$), which does not require the presence of a cation vacancy. That is, hydration in bridgmanite is not accompanied with the creation of any vacancies or any hydrogen clusters, which is in marked contrast to the previously reported hydrogen substitution mechanisms in hydrous minerals in the upper mantle, such as wadsleyite, ringwoodite, and DHMS phase E (Purevjav et al. 2014, 2016, 2018, 2020; Sano-Furukawa et al. 2011; Tomioka et al. 2016). We consider that this contrast is due to the densely packed nature of the bridgmanite structure, where larger numbers of oxygen anions coordinate a single cation. Therefore, it is energetically unfavorable to remove such a cation to create a vacancy while keeping the structure. Multiple hydrogen occupancy within one vacant site (Purevjav et al. 2014, 2016) or creation of hydrogen clusters (Purevjav et al. 2018) are prohibited in the structure of bridgmanite without vacancies, implying that its hydrogen concentration is much more limited than the upper mantle minerals, which can have numerous cation vacancies. We thus reinforce the prevailing concept that the upper mantle, including the transition zone, keeps more water than the lower mantle (Karato et al. 2020). In addition, the absence of cation vacancy in hydrous bridgmanite in the lower mantle is important for considering its rheological behavior. We confirmed the result of Muir and Brodholt (2018) by first principle calculation, where hydration of bridgmanite cannot promote hydrolytic weakening because the prevailing $Al^{3+} + H^+$ coupling mechanism does not create any cation vacancies.

It had been previously proposed that the geometry of chemical bonding around hydrogen atoms in the hydrogen-bearing deep-mantle minerals is determined with high accuracy by using smaller *d*-spacings in the TOF single-crystal experiments (Okuchi et al. 2015). Our study here demonstrates that the distances of covalent and hydrogen bonding and the angle between them can be measured even for the trace amount of hydrogen in the bridgmanite single crystal. This result opens a new window of research opportunity to analyze hydrogen positions and concentrations in other deep-mantle nominally anhydrous minerals by making full use of such neutron diffraction instruments. This type of future study can help understand the hydrogen substitution mechanism and water solubility in a wide variety of minerals in the deep Earth.

Acknowledgments

We acknowledge E. Ito at IPM for technical suggestions in high-pressure synthesis, Y. Yachi at IPM for supporting EPMA analysis, I. Miyagi at National Institute of Advanced Industrial Science and Technology for providing natural amphibole standard for SIMS, X. Wang at SNS for supporting neutron data analysis, and Wenli Bi and Ercan Alp at Argonne National Laboratory for Mössbauer analysis.

Funding

This work was supported by the Japan Society for the Promotion of Science (Post-doctoral Fellowship for Research in Japan Grant Number P17331, and KAKENHI Grant Numbers 17H01172, 18K18795, 18H04468, 20H01965 and 21H04519). J.F.L. acknowledges support from the Geophysics Program and the Cooperative Studies of The Earth's Deep Interior Program (CSEDI) of the National Science Foundation (EAR-2001381; EAR-1916941). A portion of this research at the Spallation Neutron Source was sponsored by the Scientific User Facilities Division, Office of Basic Energy Sciences, U.S. Department of Energy. This work was supported in part by the Joint Use Program at IPM, by the Kochi Core Center Open Facility System (KOFS) under the MEXT foundation, and by the collaboration research project of Integrated Radiation and Nuclear Science, Kyoto University (R3148, R4011, and R5007).

References cited

Bolfan-Casanova, N., Keppler, H., and Rubie, D.C. (2003) Water partitioning at 660 km depth and evidence for very low water solubility in magnesium silicate perovskite. Geophysical Research Letters, 30, 2003GL017182, https://doi.org/10.1029/2003GL017182.

Frost, D.J. and Langenhorst, F. (2002) The effect of Al_2O_3 on Fe-Mg partitioning between magnesiowüstite and magnesium silicate perovskite. Earth and Planetary Science Letters, 199, 227–241, https://doi.org/10.1016/S0012-821X(02)00558-7.

Fu, S., Yang, J., Karato, S.i., Vasiliev, A., Presniakov, M.Y., Gavriliuk, A.G., Ivanova, A.G., Hauri, E.H., Okuchi, T., Purevjav, N., and others. (2019) Water concentration in single-crystal (Al,Fe)-bearing bridgmanite grown from the hydrous melt: Implications for dehydration melting at the topmost lower mantle. Geophysical Research Letters, 46, 10346–10357, https://doi.org/10.1029/2019GL084630.

Fukao, Y. and Obayashi, M. (2013) Subducted slabs stagnant above, penetrating through, and trapped below the 660 km discontinuity. Journal of Geophysical Research: Solid Earth, 118, 5920–5938, https://doi.org/10.1002/2013JB010466.

Fukao, Y., Obayashi, M., and Nakakuki, T. (2009) Stagnant slab: A review. Annual Review of Earth and Planetary Sciences, 37, 19–46, https://doi.org/10.1146/annurev.earth.36.031207.124224.

Hirose, K., Fei, Y., Ono, S., Yagi, T., and Funakoshi, K. (2001) In situ measurements of the phase transition boundary in $Mg_3Al_2Si_3O_{12}$: Implications for the nature of the seismic discontinuities in the Earth's mantle. Earth and Planetary Science Letters, 184, 567–573, https://doi.org/10.1016/S0012-821X(00)00354-X.

Hirose, K., Sinmyo, R., and Hernlund, J. (2017) Perovskite in Earth's deep interior. Science, 358, 734–738, https://doi.org/10.1126/science.aam8561.

Horiuchi, H., Ito, E., and Weidner, D. (1987) Perovskite-type $MgSiO_3$: Single-crystal X-ray diffraction study. American Mineralogist, 72, 357–360.

Hummer, D.R. and Fei, Y. (2012) Synthesis and crystal chemistry of Fe^{3+}-bearing $(Mg,Fe^{3+})(Si,Fe^{3+})O_3$ perovskite. American Mineralogist, 97, 1915–1921, https://doi.org/10.2138/am.2012.4144.

Karato, S., Karki, B., and Park, J. (2020) Deep mantle melting, global water circulation and its implications for the stability of the ocean mass. Progress in Earth and Planetary Science, 7, 76, https://doi.org/10.1186/s40645-020-00379-3.

Kawakatsu, H. and Watada, S. (2007) Seismic evidence for deep-water transportation in the mantle. Science, 316, 1468–1471, https://doi.org/10.1126/science.1140855.

Kubo, A. and Akaogi, M. (2000) Post-garnet transitions in the system $Mg_4Si_4O_{12}$-$Mg_3Al_2Si_3O_{12}$ up to 28 GPa: Phase relations of garnet, ilmenite and perovskite. Physics of the Earth and Planetary Interiors, 121, 85–102, https://doi.org/10.1016/S0031-9201(00)00162-X.

Kudoh, Y., Prewitt, C.T., Finger, L.W., Darovskikh, A., and Ito, E. (1990) Effect of iron on the crystal structure of $(Mg,Fe)SiO_3$ perovskite. Geophysical Research Letters, 17, 1481–1484, https://doi.org/10.1029/GL017i010p01481.

Larson, A.C. and Von Dreele, R.B. (2004) General structure analysis system

(GSAS). Los Alamos National Laboratory Report LAUR 86-748.
Libowitzky, E. (1999) Correlation of O-H stretching frequencies and O-H···O hydrogen bond lengths in minerals. Hydrogen Bond Research, 103–115. Springer.
Libowitzky, E. and Rossman, G.R. (1997) An IR absorption calibration for water in minerals. American Mineralogist, 82, 1111–1115, https://doi.org/10.2138/am-1997-11-1208.
Lin, J.F., Mao, Z., Yang, J., Liu, J., Xiao, Y., Chow, P., and Okuchi, T. (2016) High-spin Fe^{2+} and Fe^{3+} in single-crystal aluminous bridgmanite in the lower mantle. Geophysical Research Letters, 43, 6952–6959, https://doi.org/10.1002/2016GL069836.
Litasov, K., Ohtani, E., Langenhorst, F., Yurimoto, H., Kubo, T., and Kondo, T. (2003) Water solubility in Mg-perovskites and water storage capacity in the lower mantle. Earth and Planetary Science Letters, 211, 189–203, https://doi.org/10.1016/S0012-821X(03)00200-0.
Litasov, K.D., Kagi, H., Shatskiy, A., Ohtani, E., Lakshtanov, D.L., Bass, J.D., and Ito, E. (2007) High hydrogen solubility in Al-rich stishovite and water transport in the lower mantle. Earth and Planetary Science Letters, 262, 620–634, https://doi.org/10.1016/j.epsl.2007.08.015.
Liu, Z., Fei, H., Chen, L., McCammon, C., Wang, L., Liu, R., Wang, F., Liu, B., and Katsura, T. (2021) Bridgmanite is nearly dry at the top of the lower mantle. Earth and Planetary Science Letters, 570, 117088, https://doi.org/10.1016/j.epsl.2021.117088.
Meade, C., Reffner, J.A., and Ito, E. (1994) Synchrotron infrared absorbance measurements of hydrogen in $MgSiO_3$ perovskite. Science, 264, 1558–1560, https://doi.org/10.1126/science.264.5165.1558.
Miyagi, I. and Yurimoto, H. (1995) Water content of melt inclusions in phenocrysts using secondary ion mass spectrometer. Bulletin of the Volcanological Society of Japan, 40, 349–355.
Momma, K. and Izumi, F. (2011) VESTA3 for three-dimensional visualization of crystal, volumetric and morphology data. Journal of Applied Crystallography, 44, 1272–1276, https://doi.org/10.1107/S0021889811038970.
Muir, J.M.R. and Brodholt, J.P. (2018) Water distribution in the lower mantle: Implications for hydrolytic weakening. Earth and Planetary Science Letters, 484, 363–369, https://doi.org/10.1016/j.epsl.2017.11.051.
Murakami, M., Hirose, K., Yurimoto, H., Nakashima, S., and Takafuji, N. (2002) Water in Earth's lower mantle. Science, 295, 1885–1887, https://doi.org/10.1126/science.1065998.
Nakatsuka, A., Fukui, H., Kamada, S., Hirao, N., Ohkawa, M., Sugiyama, K., and Yoshino, T. (2021) Incorporation mechanism of Fe and Al into bridgmanite in a subducting mid-ocean ridge basalt and its crystal chemistry. Scientific Reports, 11, 22839, https://doi.org/10.1038/s41598-021-00403-6.
Navrotsky, A. (1999) A lesson from ceramics. Science, 284, 1788–1789, https://doi.org/10.1126/science.284.5421.1788.
Nishio-Hamane, D., Nagai, T., Fujino, K., Seto, Y., and Takafuji, N. (2005) Fe^{3+} and Al solubilities in $MgSiO_3$ perovskite: Implication of the $Fe^{3+}AlO_3$ substitution in $MgSiO_3$ perovskite at the lower mantle condition. Geophysical Research Letters, 32, L16306, https://doi.org/10.1029/2005GL023529.
Ohtani, E., Litasov, K., Hosoya, T., Kubo, T., and Kondo, T. (2004) Water transport into the deep mantle and formation of a hydrous transition zone. Physics of the Earth and Planetary Interiors, 143–144, 255–269, https://doi.org/10.1016/j.pepi.2003.09.015.
Okuchi, T., Purevjav, N., Tomioka, N., Lin, J.-F., Kuribayashi, T., Schoneveld, L., Hwang, H., Sakamoto, N., Kawasaki, N., and Yurimoto, H. (2015) Synthesis of large and homogeneous single crystals of water-bearing minerals by slow cooling at deep-mantle pressures. American Mineralogist, 100, 1483–1492, https://doi.org/10.2138/am-2015-5237.
Panero, W.R., Pigott, J.S., Reaman, D.M., Kabbes, J.E., and Liu, Z. (2015) Dry $(Mg,Fe)SiO_3$ perovskite in the Earth's lower mantle. Journal of Geophysical Research: Solid Earth, 120, 894–908, https://doi.org/10.1002/2014JB011397.
Pearson, D.G., Brenker, F.E., Nestola, F., McNeill, J., Nasdala, L., Hutchison, M.T., Matveev, S., Mather, K., Silversmit, G., Schmitz, S., and others. (2014) Hydrous mantle transition zone indicated by ringwoodite included within diamond. Nature, 507, 221–224, https://doi.org/10.1038/nature13080.
Portner, D.E., Rodríguez, E.E., Beck, S., Zandt, G., Scire, A., Rocha, M.P., Bianchi, M.B., Ruiz, M., França, G.S., Condori, C., and Alvarado, P. (2020) Detailed structure of the subducted Nazca slab into the lower mantle derived from continent-scale teleseismic P wave tomography. Journal of Geophysical Research: Solid Earth, 125, e2019JB017884.
Prescher, C., McCammon, C., and Dubrovinsky, L. (2012) MossA: A program for analyzing energy-domain Mössbauer spectra from conventional and synchrotron sources. Journal of Applied Crystallography, 45, 329–331, https://doi.org/10.1107/S0021889812004979.
Purevjav, N., Okuchi, T., Tomioka, N., Abe, J., and Harjo, S. (2014) Hydrogen site analysis of hydrous ringwoodite in mantle transition zone by pulsed neutron diffraction. Geophysical Research Letters, 41, 6718–6724, https://doi.org/10.1002/2014GL061448.
Purevjav, N., Okuchi, T., Tomioka, N., Wang, X., and Hoffmann, C. (2016) Quantitative analysis of hydrogen sites and occupancy in deep mantle hydrous wadsleyite using single crystal neutron diffraction. Scientific Reports, 6, 34988, https://doi.org/10.1038/srep34988.
Purevjav, N., Okuchi, T., Wang, X., Hoffmann, C., and Tomioka, N. (2018) Determination of hydrogen site and occupancy in hydrous Mg_2SiO_4 spinel by single-crystal neutron diffraction. Acta Crystallographica Section B, 74, 115–120, https://doi.org/10.1107/S2052520618000616.
Purevjav, N., Okuchi, T., and Hoffmann, C. (2020) Strong hydrogen bonding in a dense hydrous magnesium silicate discovered by neutron Laue diffraction. IUCrJ, 7, 370–374, https://doi.org/10.1107/S2052252520003036.
Ross, N.L. and Hazen, R.M. (1989) Single crystal X-ray diffraction study of $MgSiO_3$ perovskite from 77 to 400 K. Physics and Chemistry of Minerals, 16, 415–420, https://doi.org/10.1007/BF00197010.
Sano-Furukawa, A., Kuribayashi, T., Komatsu, K., Yagi, T., and Ohtani, E. (2011) Investigation of hydrogen sites of wadsleyite: A neutron diffraction study. Physics of the Earth and Planetary Interiors, 189, 56–62, https://doi.org/10.1016/j.pepi.2011.07.003.
Sano-Furukawa, A., Hattori, T., Komatsu, K., Kagi, H., Nagai, T., Molaison, J.J., Dos Santos, A.M., and Tulk, C.A. (2018) Direct observation of symmetrization of hydrogen bond in δ-AlOOH under mantle conditions using neutron diffraction. Scientific Reports, 8, 15520, https://doi.org/10.1038/s41598-018-33598-2.
Schultz, A.J., Jørgensen, M.R.V., Wang, X.P., Mikkelson, R.L., Mikkelson, D.J., Lynch, V.E., Peterson, P.F., Green, M.L., and Hoffmann, C.M. (2014) Integration of neutron time-of-flight single-crystal Bragg peaks in reciprocal space. Journal of Applied Crystallography, 47, 915–921, https://doi.org/10.1107/S1600576714006372.
Shimizu, K., Ushikubo, T., Hamada, M., Itoh, S., Higashi, Y., Takahashi, E., and Ito, M. (2017) H_2O, CO_2, F, S, Cl, and P_2O_5 analyses of silicate glasses using SIMS: Report of volatile standard glasses. Geochemical Journal, 51, 299–313, https://doi.org/10.2343/geochemj.2.0470.
Spektor, K., Nylen, J., Mathew, R., Edén, M., Stoyanov, E., Navrotsky, A., Leinenweber, K., and Häussermann, U. (2016) Formation of hydrous stishovite from coesite in high-pressure hydrothermal environments. American Mineralogist, 101, 2514–2524, https://doi.org/10.2138/am-2016-5609.
Sugahara, M., Yoshiasa, A., Komatsu, Y., Yamanaka, T., Bolfan-Casanova, N., Nakatsuka, A., Sasaki, S., and Tanaka, M. (2006) Reinvestigation of the $MgSiO_3$ perovskite structure at high pressure. American Mineralogist, 91, 533–536, https://doi.org/10.2138/am.2006.1980.
Suzuki, A., Ohtani, E., Kondo, T., Kuribayashi, T., Niimura, N., Kurihara, K., and Chatake, T. (2001) Neutron diffraction study of hydrous phase G: Hydrogen in the lower mantle hydrous silicate, phase G. Geophysical Research Letters, 28, 3987–3990, https://doi.org/10.1029/2001GL013260.
Thompson, A.B. (1992) Water in the Earth's upper mantle. Nature, 358, 295–302, https://doi.org/10.1038/358295a0.
Tomioka, N., Okuchi, T., Purevjav, N., Abe, J., and Harjo, S. (2016) Hydrogen sites in the dense hydrous magnesian silicate phase E: A pulsed neutron powder diffraction study. Physics and Chemistry of Minerals, 43, 267–275, https://doi.org/10.1007/s00269-015-0791-4.
Townsend, J.P., Tsuchiya, J., Bina, C.R., and Jacobsen, S.D. (2016) Water partitioning between bridgmanite and postperovskite in the lowermost mantle. Earth and Planetary Science Letters, 454, 20–27, https://doi.org/10.1016/j.epsl.2016.08.009.
Trots, D.M., Kurnosov, A., Manthilake, M.A.G.M., Ovsyannikov, S.V., Akselrud, L.G., Hansen, T., Smyth, J.R., and Frost, D.J. (2013) The determination of hydrogen positions in superhydrous phase B. American Mineralogist, 98, 1688–1692, https://doi.org/10.2138/am.2013.4475.
Zikovsky, J., Peterson, P.F., Wang, X.P., Frost, M.J., and Hoffmann, C. (2011) CrystalPlan: An experiment-planning tool for crystallography. Journal of Applied Crystallography, 44, 418–423, https://doi.org/10.1107/S0021889811007102.

Manuscript received June 20, 2022
Manuscript accepted August 6, 2023
Accepted manuscript online August 18, 2023
Manuscript handled by Jennifer Kung

Endnote:

[1]Deposit item AM-24-68680. Online Materials are free to all readers. Go online, via the table of contents or article view, and find the tab or link for supplemental materials. The CIF has been peer-reviewed by our Technical Editors.